Nanoarchitectonics of Lead-Free 2D Cobalt-Based Diammonium Hybrid for Perovskites Solar Cell Applications

Mansour Abdulrhman[a], Seham K. Abdel-Aal[b, c*], Connor Alexander Bain[a], Dimitrios Raptis[c], Francisco Bernal-Texca[c], Krystian L. Wlodarczyk[d], Duncan P. Hand[d], Jordi Martorell[c, *], Jose Marques-Hueso[a,e, *]

[a] School of Engineering and Physical Sciences, Institute of Sensors, Signals and Systems, Heriot-Watt University, EH14 4AS, Edinburgh, United Kingdom

[b] Physics department, faculty of Science, Cairo University, 12613, Giza, Egypt. E-mail: seham@sci.cu.edu.eg

[c] ICFO–Institut de Ciències Fotòniques , The Barcelona Institute of Science and Technology Castelldefels, Barcelona 08860, Spain E-mail; jordi.martorell@icfo.es,

[d] School of Engineering and Physical Sciences, Institute of Photonics and Quantum Sciences, Heriot-Watt University, EH14 4AS, Edinburgh, United Kingdom

[e] ICMUV-Institute for Materials Science, University of Valencia, 46980 Paterna, Spain. E-mail: Jose.Marques@uv.es

Abstract

This study presents the fabrication of new, non-toxic perovskite solar cells using 2D cobalt-based perovskite materials. Three cobalt-based Organic-inorganic 2D hybrid perovskite (HOIP) materials were synthesized, and their photovoltaic properties were evaluated: $[NH_3(CH_2)nNH_3]CoCl_4$ (n= 4, 9) and $[NH_3(CH_2)_7NH_3]CoBr_2Cl_2$. These materials encompassed varying organic chain lengths (short, medium, and long) as well as chloride and mixed chloride/bromide anions. The molecular structure was examined to establish correlations with the structural and optical properties. The synthesized compounds exhibited visible light absorption, with varying bandgap energy from 1.7 eV to 2.7 eV. To test the application of Co-based perovskites, two distinct solar cell architectures were employed. The first architecture, denoted as Architecture 1, consisted of the following layers: Glass/FTO/c-TiO_2/m-TiO_2/ZrO_2/2D Co-based HOIP/C-electrode. The second architecture, referred to as Architecture 2, utilized a planar heterojunction structure deposited with different transport layers for electrons and holes. Specifically, it comprised the layers: Glass/ITO/SnO_2/2D Co-based HOIP/Spiro-OMeTAD/Au. Among these architectures, Architecture 2 exhibited notable performance. It achieved a maximal open circuit voltage (Voc) of 0.93 V, and current density (Jsc) of 0.24 mA/cm^2, with efficiency of 0.47 %, and a fill factor (FF) of 78 %. These findings demonstrate the effectiveness of adjusting the perovskite material composition and controlling the deposition conditions in raising solar cell efficiency.

Keywords: lead–free perovskites, 2D hybrid perovskites, HOIPs, perovskite solar cell

1. Introduction

Perovskite solar cells have experienced an increase in light power conversion efficiency (PCE) from 3 % in 2008 to around 25.7 % in 2022, fuelled by a growing interest in perovskite materials in the research field [1]. This remarkable progress has positioned perovskite solar cells as a viable competitor to silicon solar cell varieties [2]. Perovskite solar cells offer advantages such as tunable wavelength, suitable bandgap, synthesis from chemical solutions, and rapid deposition onto thin films. However, challenges related to toxicity and chemical stability still need to be addressed [2], [3]. Additionally, some perovskite materials can chemically react under ambient conditions, leading to degradation of their properties [4].

The conventional structure of perovskites follows the ABX_3 format, where an organic cation occupies the A site, a metal cation (typically lead, Pb) occupies the B site, and an anion occupies the X site [2]. Although lead-based perovskites are extensively researched, their primary drawback is the toxicity of lead, which poses environmental and health risks. Consequently, the translation of lead-based perovskites into large-scale production and commercialization is impeded [5]. Therefore, finding lead-free alternatives has become crucial. Several approaches have been explored, including replacing lead with tin (Sn), germanium (Ge), or bismuth (Bi) [6]. However, lead-free alternatives still face challenges in achieving high power conversion efficiency (PCE) compared to lead-based perovskites [7]. To address this issue, researchers have focused on reducing the dimensionality of perovskite structures from 3D to 2D, including the use of 0D quantum dots perovskites [8]. It has been demonstrated that 2D perovskites exhibit improved properties, such as reduced trap density in the film [9].

Among the various 2D perovskites investigated, hybrid organic-inorganic perovskites have garnered significant attention. These materials combine the advantages of organic and inorganic components within each molecule, offering improved resistance to moisture, broader bandgap, and enhanced structural stability [10]. Compared to 3D perovskites, 2D perovskites exhibit greater stability [11] as chemical stability tends to increase at lower dimensions [12]. Simply stated, the size of 3D crystal perovskites is reduced into 2D nanocrystals to make 2D perovskites. [13]. Various methods have been reported to synthesize 2D perovskites, including the Riddlesden-Popper phase, which features a two-dimensional structure with the chemical formula $A_{n+1}B_nX_{3n+1}$ [14], where $nABX_3$ layers are sandwiched between two AX rock-salt layers. The energy levels of this type of perovskite correspond to assembled quantum wells [15]. These unique optical properties make 2D perovskites suitable for applications in optical electronics, smart microelectronics, and green solar cell production [16].

Recent studies have focused on synthesizing and characterizing 2D cobalt-based perovskites with the chemical structure $[(NH_3)(CH_2)_n(NH_3)]CoCl_xBr_{4-x}$ [17]. These structures comprise an organic anionic ammonium salt with different organic chain lengths $[NH_3(CH_3)_nNH_3]$ (where n = 4,5,6,7,9), while the inorganic cation CoX_4 is located between two layers of the organic cation in the 2D structure with

organic and inorganic components connected via hydrogen bonding. The crystal structure, vibration spectroscopy and physical properties can be found in the references [14], [16], [18], [19]. Co (II) hybrids of diprotonated hydrocarbon chains, e.g. $[(CH_2)_n(NH_3)_2]CoCl_4$; n = 4 - 12, have also been prepared, and it has been shown that tuning the physical properties of cobalt-based perovskites has been achieved through variations in the structure, chain length, and halide composition [20]–[25].

Considerable attempts have been made to advance and develop lead-free perovskite solar cells with comparable performance and energy conversion to lead-based compounds. Lead-free alternatives, such as Sn-based [27], Ge-Sn-based [28], and Ge-based perovskites [29], have shown inadequate chemical stability without encapsulation in ambient or humid environments [30]. However, surface defects have also been identified as a limitation in Bi-based perovskites, leading to quenching and reduced performance [31]. Nevertheless, PCE in lead-free perovskites has steadily improved from 0.003 % to 3.59 % [32].

One promising alternative to lead-based perovskite is $MAGeI_3$, a Ge-based organic-inorganic hybrid. With a fill factor of ~1 and a bandgap of ~1.6 eV, $MAGeI_3$ is being explored for solar cells due to its desirable properties and improved chemical stability in ambient air [33]. Substituting larger cations like Cs achieves a direct bandgap of ~1.7 eV with good thermal stability [34], [35]. Another modification involves replacing some iodide ions with bromide ions to form $MAGeI_{2.7}Br_{0.3}$, enhancing optical properties and perovskite performance [35], [36]. Additionally, the 2D structure $(PEA)_2Ge_{1-x}Sn_xI_4$, especially $(PEA)_2Ge_{0.5}Sn_{0.5}I_4$, exhibits superior stability in ambient air compared to 3D $MAGeI_3$, making it a promising candidate for photovoltaic applications [37].

Other cost-effective materials, such as cobalt and copper, have gained attention for their possible applications in perovskite solar cells [38]. In the case of copper, specifically Cu^+, it offers advantages due to its low toxicity [39]. With a smaller ionic radius than lead, copper possesses 78 pm for Cu^+ and 199 pm for Pb_2^+, respectively, while Sn_2^+ has an ionic radius of 110pm [40]. Copper-based perovskites are often fabricated in a 2D structure and are typically synthesized with structure $(CH_3NH_3)_2CuX_4$,where X represents a halogen, and the divalent CH_3NH_3 can be substituted by an aliphatic component [40]. These 2D perovskites have shown relatively low efficiencies of approximately 2.4 % and a Voc of 0.56V with 0.59 FF achieved for $(CH_3NH_3)_2CuCl_4$. However, further structural modifications have been made to enhance stability in ambient conditions by reducing the amount of Cl^- and creating $(CH_3NH_3)_2CuCl_2I_2$, resulting in lower values of Jsc at 6.78 mA/cm^2, Voc at 0.54V and efficiency at 1.75 % [41].

Bismuth perovskite $MABiX_3$, particularly I_2S or I_2Se, is non-toxic and exhibits favourable optical properties for photovoltaics. A mixed cation Bi-based perovskite, $MABiI_2S$, with a suitable bandgap of 1.56 eV and exhibits high absorption up to 1000 nm, indicating its potential as an effective photovoltaic material [42]. The deposition process have an important role in the fabrication of $MA_3Bi_2I_9$ perovskite

devices, where the material concentration significantly affects the resulting performance [43]. The device exhibited an efficiency of 0.17 % and a Voc of approximately 0.73 V for spin-coating fabrication. The solution can be entirely manufactured using three distinct methods: dipping, spraying, and spinning. From there, the spinning method has shown better performance and morphology [44].

Cobalt has recently emerged as a potential alternative due to its excellent electrical and magnetic properties [23]–[25]. A study by Matthew T. Klug et al. partially replaced 6 % of Pb with Co-fabricating MAPb-CoI_3, improving efficiency from 14.5 % to 15 % [45]. In addition, cobalt-based perovskites are prepared as a solution-based material, which allows various deposition techniques, including spin coating, spray coating followed by thermal annealing to be used. This allows for greater control over the resulting morphology and performance of the devices [46]–[48].

This study focuses on the fabrication of solar cell devices using Co (II) diammonium hybrid organic-inorganic perovskites (HOIPs). The deposition uses three different 2D cobalt-based hybrid perovskites with varying organic chain lengths and halide compositions of the formula ($[NH_3(CH_2)_4NH_3]CoCl_4$, $[NH_3(CH_2)_7NH_3]CoBr_2Cl_2$, and $[NH_3(CH_2)_9NH_3]CoCl_4$). The use of Co-based perovskites is tested in two different solar cell architectures: mesoporous hole transport layer-free (glass/FTO/c-TiO_2/m-TiO_2/ZrO_2/Co-HOIPs/Carbon electrode) and planar heterostructure devices (Glass /ITO/SnO_2/2D Co-HOIP/Spiro-OMeTAD/ Au). The resulting solar cells demonstrate efficiencies of 0.47 % and 0.16 %, with fill factor values of 0.78 and 0.67, which are good values among lead-free low-cost hybrid perovskites. The results show the significance of selecting suitable architecture for Co-based perovskite devices to achieve best performance. Controlling deposition parameters and optimising the composition of materials broaden the possibility of fabricating high performance lead-free perovskite solar cell with enhanced efficiency.

2. Procedures

2.1 Material Synthesis

All chemicals were purchased from SIGMA-ALDRICH and used without any further modification, with all product purities exceeding 98 %. Solvents were of reagent grade. Synthesis of $[NH_3(CH_2)_nNH_3]CoCl_4$, n= 4, 9 and $[NH_3(CH_2)_7NH_3]CoBr_2Cl_2$ (in short 2C4CoCl, 2C9CoCl and 2C7CoCB) in powder and single crystals were previously reported [20]–[26]. In short, an ethanoic solution of diammonium salts was mixed in a 1:1 molar ratio with $CoCl_2$ at T= 60 °C at constant stirring for 30 min, then cooled down and kept in a desiccator until the blue crystals of perovskite precipitated upon gradual cooling to room temperature.

2.2 Characterisation

2.2.1 Morphological Characterization.

The Co-based perovskite materials were spin-coated on a glass substrate and sputtered with gold for morphological inspection with a scanning electron microscope (SEM), specifically the JSM 6510 LV JEOL model. Particle size distribution was obtained by analysing transmission electron microscopy (TEM) images using ImageJ particle analysis. The TEM images were captured using a JEM 2100 JEOL microscope, and the samples were deposited on a copper grid after scrapping.

The X-ray diffraction (XRD) patterns were obtained using a Enraf-Nonius 590 Kappa CCD single crystal diffractometer with graphite monochromator using MoKa (0.71073 Å). Powders from the samples were deposited on a XRD holder.

2.2.2 Optical Spectra

Optical characterization was conducted using a UV-visible spectrophotometer, specifically the lambda Perkin Elmer (PE) Lambda XLS spectrometer. The absorbance spectra of Co-based perovskite were measured using this instrument. The optical bandgap was calculated using the Kubelka-Munk formula to transform the measured reflectance spectra to the corresponding absorption spectra [16]. Details on applying the Kubelka-Munk function can be found in reference [49].

2.2.3 Current-Voltage -V curves Characterisation

For Architecture 1 (glass/FTO/c-TiO_2/m-TiO_2/ZrO_2/Co-HOIPs/Carbon electrode), the current-voltage (J-V) characteristics of Co-based perovskite devices were obtained by exposing the samples to a light intensity of 1000 W/m^2 from a solar simulator (ABET Technologies Sun 2000 solar simulator). Data acquisition was performed through a TCS-RO3 I-V tracer, with a time setting scan of 100 mV/s which is equivalent to the standard solar irradiance of AM 1.5G Sun. Full sun illumination was employed, allowing light to penetrate through the substrate, maximizing light absorption within the perovskite layer. 20 minutes were allowed between measurements.

For architecture 2 (Glass/ITO/SnO_2/2D Co-HOIP/Spiro-OMeTAD/Au), the current-voltage (J-V) characteristics of Co-based perovskite devices were measured by illuminating the glass side of the samples with a light intensity of 1000 W/m^2 from a sunlight solar simulator (Sun 3000, Abet Technologies) with light intensity equivalent to the standard solar irradiance of AM 1.5G Sun. The solar simulator was connected to a Keithley 2400 SourceMeter for data acquisition.

2.3. Solar cell fabrication based 2D- Co hybrid perovskites.

The use of Co-based perovskites is tested in two different solar cell architectures outlined as follows:

2.3.1 Architecture1: Hole transport layer-free (glass/FTO/c-TiO_2/m-TiO_2/ZrO_2/Co-HOIPs/Carbon electrode).

To create a more uniform distribution of the perovskite solar cell layers, which is important for the device functionality, a square (20 x 15 mm) fluorine-doped tin oxide (FTO) glass substrates with a thickness of 1.1 mm were machined using a 35 W Tangerine ultrashort pulse laser (Amplitude Systèmes, France) to remove the conductive thin film from two 0.4 mm broad areas. The laser-machined areas were 1.4 mm apart, the first approximately 5 mm from the glass edge. The ablation of the conductive thin film was done by raster-scanning the areas with an infrared laser beam (1032 nm wavelength) with a 30 μm diameter. The laser pulse duration was 260 fs, pulse energy 47.5 μJ, pulse repetition rate 35 kHz, laser scan speed 175 mm/s, and hatch distance 5 μm. After applying for five laser passes, the laser beam ablated approximately 10 μm layer of glass along with the conductive thin film, patterning the FTO substrates to form two electrodes. The substrate was cleaned in DI water and two drops of Hellmanex in an ultrasonic bath for 15 min, then rinsed twice with DI water. Then, it was cleaned in the ultrasonic bath for 15 min IPA and cleaned with DI water. The precursor solution for the compact titanium layer (C-TiO_2) consisted of 0.23 M titanium isopropoxide (Sigma-Aldrich, 99.999 %) and 0.013 M hydrochloric acid (HCl) solution in isopropanol (99.5 % Fisher Chemicals). To prepare the C-TiO_2 solution, 369 ml of titanium isopropoxide was added to 2.53 ml of isopropanol, resulting in a concentration of 0.46 M. Additionally, a separate solution was created by diluting 35 ml of a 2 M HCl solution with 2.53 ml of isopropanol, resulting in a concentration of 0.026 M. The diluted acid solution was then combined with the titanium precursor solution under vigorous stirring. Prior to usage, the resulting mixture was filtered using a PTFE filter with a pore size of 0.2 μm. The C-TiO_2 solution was deposited onto the etched and cleaned FTO substrates through spin-coating at 2000 revolutions per minute (r.p.m.) for 60 seconds, followed by heating at 500 °C for 30 minutes, which gave a thickness of 40 μm [50], [51] The mesoporous titanium (M-TiO_2) layer was created by diluting the TiO_2 paste with absolute ethanol in a weight ratio of 1:9. A 50 μl solution of mesoporous TiO_2 (mp-TiO_2) was applied to the substrate and evenly coated by spinning at 2000 rpm for 20 seconds. Subsequently, it was dried at 120 °C for 10 minutes and further heated at 500 °C for 30 minutes, resulting in a thickness of approximately 300 nm [51], [52]. For the preparation of the zirconia nanoparticles solution, ZrO_2 was

combined with n-propanol, HCl, and DI water in a sequential molar ratio of 25:2:1:1 (n-propanol: Zr precursor: HCl: DI water). The mixture was stirred at room temperature until a clear suspension was achieved [53]. After that, ultrasonication was performed to ensure complete dispersion of the ZrO_2 particles. ZrO_2 solution was spin-coated at 2000 rpm [54], then dried in an oven at 120 °C, followed by 500 °C for 30 min [55], giving a thickness of 450 nm [56]. 10 g of carbon black and graphite powder (Sigma–Aldrich), mixed with a 3:7 weight ratio, mixed with 10 ml DI water until homogeneously mixed. The area covered with the samples was masked with adhesive polyimide cutting shapes to avoid any presence of perovskite material anywhere other than the active area. After applying conductive carbon paste, the carbon electrodes were coated by doctor blading with an active area of 1cm x1cm layer thickness of about 8 µm [57], [58]. The thickness of the layer was measured using a KLA-Tencor P-7 profilometer. Co-based perovskite solution was kept in water-bath at 70 °C for 1 hour prior to the process. 5 µL of Co-based perovskite was dispensed on the surface. Gradual infiltration of the liquid into the porous structure, resulting in the displacement of the liquid dome with wet casting. Visual inspection through the glass substrate should demonstrate the comprehensive wetting of the entire stack, extending downward to the device layers, then thermally annealed at 65 °C for one hour in vacuum [51] [56]. The process is shown in Figure 1(a).

2.3.2 Architecture 2: Glass /ITO/SnO_2/2D Co- HOIP/Spiro-OMeTAD/ Au)

Solar cells featuring a planar heterojunction (PHJ) configuration were produced following a specific layer arrangement: Glass/ITO/SnO_2/2D Co-HOIP/Spiro-OMeTAD/Au. The layers were assembled as illustrated in Figure 1(b). ITO substrates possessing a sheet resistance of 15 Ω sq^{-1} were divided into 30 × 30 mm sections. These substrates underwent a sequential cleaning process in an ultrasonic bath employing acetone, isopropyl alcohol, and deionized water, with each step lasting 10 minutes. After drying, UV-ozone treatment was applied to the substrates for 10 minutes. The electron transport layer was deposited by spin-coating 180 µl of 5 % SnO_2 at 3200 rpm for 30 s, followed by annealing at 150 °C for 30 min, resulting in a thickness of 100 nm. The 2C9CoCl and 2C7CoCB perovskite precursor solutions were made by combining 45 mg of each in 330 µL of (DMF: DMSO) (4:1 v/v) and stirring for 24 hours. The perovskite films were applied to the substrates by spin-coating, which involved injecting 80 µl of the solution, spin-coating it at 2000 rpm for 30 s, and then annealing it at 70 °C for 10 min. resulting in a thickness of 300 nm. The films were then transferred to a glovebox containing a nitrogen atmosphere. The hole transport layer (Spiro) was spin-coated using 80 µl and 4000 rpm for 30 s, achieving an 80 nm thickness. The films were left in a desiccator overnight, and thermal evaporation was used to deposit 100 nm gold layer, as described in Figure 1(b).

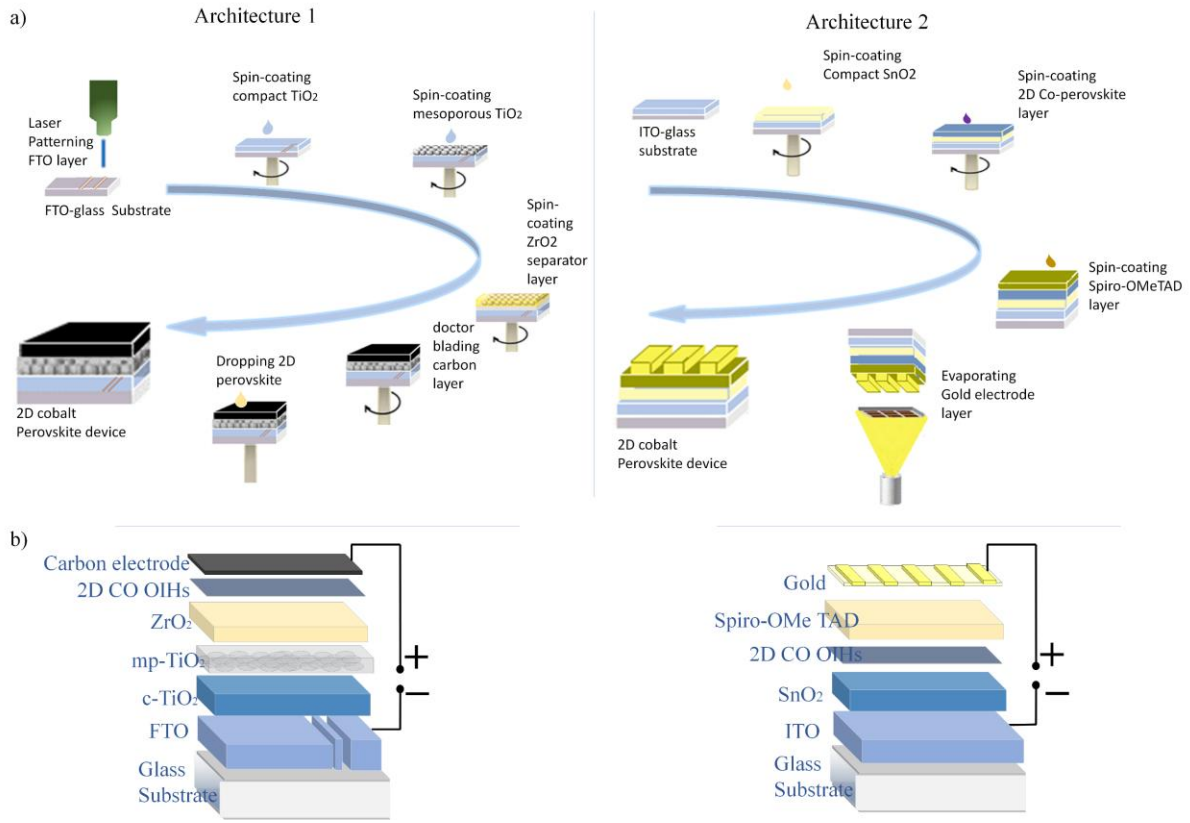

Figure 1: (a) Graphical representation of the steps for device production for both Architectures and (b) Cross-sectional schematic diagram of Co-based HOIP devices architectures.

3. Results and discussions

3.1 Structure description of $[NH_3(CH_2)_nNH_3]CoCl_4$ n= 4, 9 and $[NH_3(CH_2)_7NH_3]CoCl_2Br_2$

X-ray diffraction (XRD) patterns unveil the atomic arrangements within the synthesized compounds. In the low-angle region (5-12°), subtle peaks suggest the presence of organic chains in 2C4CoCl, progressively diminishing in 2C7CoCB and 2C9CoCl, illustrating the increasingly disordered nature with larger organic chain length (n = 4, 7, 9). A notable peak at 19-21° is present in all three XRD patterns, originating from the robust tetrahedral coordination of Co-Cl bonds in 2C4CoCl and 2C9CoCl. In 2C7CoCB, it represents a combination of Co-Cl and Co-Br bonds, highlighting the coexistence of both halides. Medium-sized peaks in the 25-30° and 24-30° ranges for 2C4CoCl and 2C7CoCB, respectively, provide insights into the molecular arrangements within the crystalline lattice. Weaker peaks at 35-40° in all three patterns indicate higher-order reflections, supporting the validity of the overall crystal structure model.

The chemical formula A_2CoX_4 indicates a 2D organic-inorganic hybrid perovskite, as reported by our group and elsewhere [20]–[26]. The triclinic crystal structure of the 2D perovskite hybrid $NH_3(CH_2)_nNH_3CoCl_4$ (n = 4, 9) (denoted 2C4CoCl and 2C9CoCl), and the mixed halide

$[NH_3(CH_2)_7NH_3]CoCl_2Br_2$ hybrids (denoted 2C7CoCB) contain organic cations $^+NH_3(CH_2)_nNH_3^+$ and inorganic anions $CoCl_4^{2-}$ regardless of aliphatic organic chain lengths.

The organic ion consists of 4, 7 or 9 carbon atoms disposed of in a zigzag structure with two ammonium groups (NH_3) attached at the ends. The hydrogen bonds [H---N---Cl] connect the hydrogen to the ends of the diammonium organic part with the chlorine attached to the inorganic part (cobalt chloride) to form an organic-inorganic-organic cohesion layered structure. The cobalt chloride ion forms isolated distorted tetrahedral structures quasi zero-dimensional. The three OIHs are crystallised in a triclinic $P\bar{1}$ space group with two molecules per unit cell. The unit cell parameters for the three materials are shown in Table (1). The details of the structure description and hydrogen bond lengths are described in our previous work [20-26]. The structure information can be obtained from the Cambridge Crystallographic Data Center via deposit number CCDC for 2C4CoCl (1401386), 2C7CoCB (80518) and 2C9CoCl (14378.13), respectively. Figure (2) shows the arrangement of $[CoCl_4]^{2-}$ tetrahedra in the b-direction, indicating an alternate tetrahedral arrangement. The structure is described as naturally self-assembled. The organic layer and inorganic layer thicknesses are shown in Table (2). The XRD and molecular arrangement of each compound are shown in Figure (2), where the grey atom is carbon, white for H, green for chlorine and light blue for nitrogen, dark blue for cobalt, and brown for bromine.

Table (1) Unit cell dimensions of 2C9CoCl, 2C4CoCl and 2C7CoCB

Formula	**A (Å)**	**B (Å)**	**C (Å)**	**α(°)**	**β (°)**	**γ(°)**	**V (Å^3)**	**sp. gr**	**Z**	**Ref**
2C4CoCl	7.2869	8.150	10.412	77.295	80.058	82.837	591.81	$P\bar{1}$	2	[17]
2C7CoCB	7.3107	10.1841	11.269	66.810	78.858	87.664	756.10	$P\bar{1}$	2	[24]
2C9CoCl	7.3113	10.2373	12.4701	112.323	92.441	93.452	859.68	$P\bar{1}$	2	[25]

Table (2) Unit cell parameters of 2C9CoCl, 2C4CoCl and 2C7CoCB

formula structure	**$[CoCl]^{2-}$ layer thickness A**	**$^+NH_3(CH_2)_nNH_3^+$ n=4, 7, 9 layer thickness A**	**Hydrogen bond length N---H---Cl**
2C4CoCl	3.68, 3.65	6.27,	2.3 Å
2C7CoCB	3.94 Br-Br, 3.85 Cl-Cl	8.94,	2.7 Å
2C9CoCl	3.65, 3.76	11.63	2.9 Å

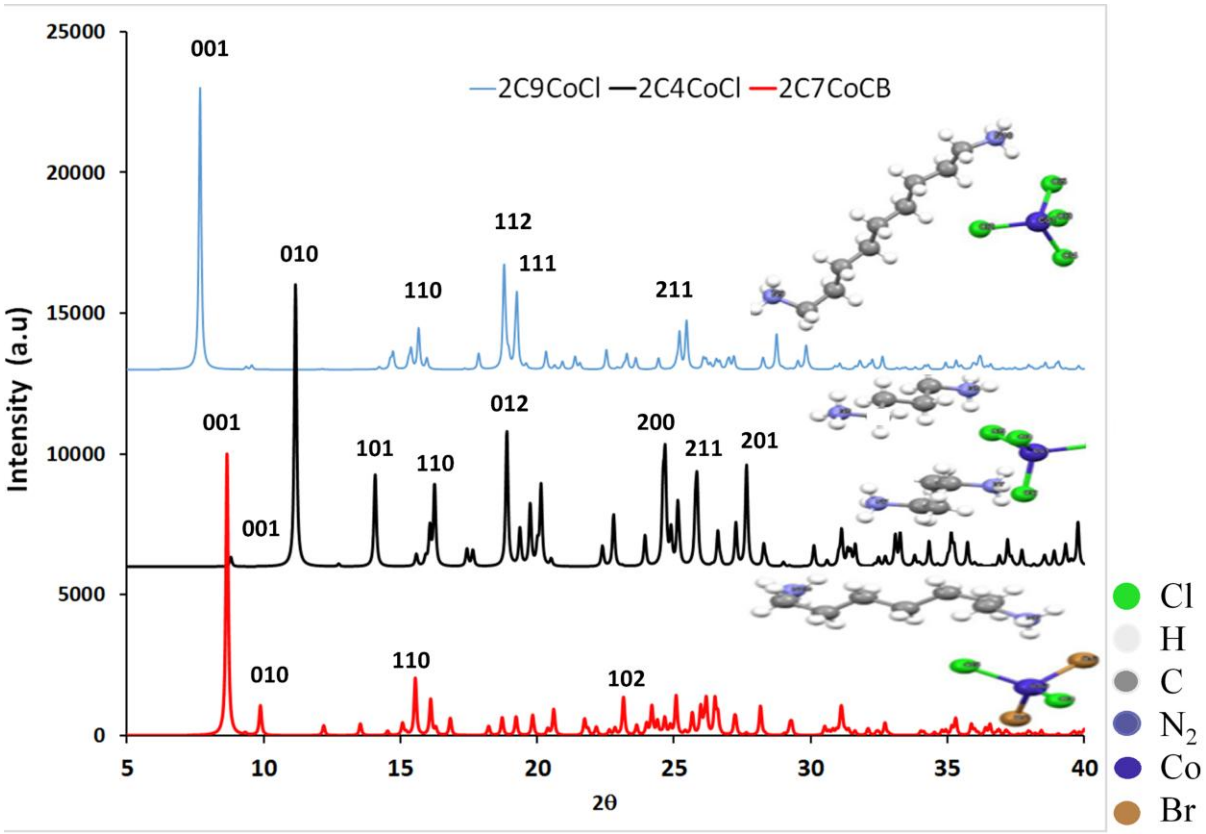

Figure 2. XRD diffraction pattern of 2C9CoCl, 2C4CoCl and 2C7CoCB, with the molecular arrangement of each shown in the inset.

3.2 Morphology and particle size measurement.

Figure 3 presents the scanning electron microscopy (SEM) images of the different 2C4CoCl short chain lengths, 2C7CoCB, and 2C9CoCl films. The SEM images reveal the morphology of the surfaces, including cracks observed in the 2C4CoCl films, which may result from the deposition process or the material composition [59]. Figure 3 (b-c) presents SEM images of the different 2C7CoCB and 2C9CoCl films. The 2D perovskite films typically exhibit excellent quality and morphology, facilitating device fabrication. [59]. Both compounds exhibit a flaky morphology, with flake sizes ranging from 400 nm to 1 µm, and clear boundaries visible in the SEM images. However, 2C9CoCl shows a less homogeneous size distribution and grains with undefined boundaries on its surface. Conversely, the morphology of 2C7CoCB reveals larger flakes, potentially attributed to the introduction of bromide [60]. Figure 3(d) demonstrates that compound 2C4CoCl exhibits a more monodisperse particle size distribution, with uniform particle sizes below 16 nm. Shorter chain lengths result in smaller particles, with an average size of approximately 10 nm. TEM images in Figure 3(e-f) showcase the morphology and particle size distribution of 2C7CoCB and 2C9CoCl HOIPs. The particle size is strongly influenced by the chain length. For 2C7CoCB, a more monodisperse size distribution is observed, with uniform particle sizes ranging from 20 nm to 5 nm. Only a few particles with smaller sizes were found, with an

average size of 14.2 nm. In contrast, 2C9CoCl perovskites exhibit more polydisperse sizes, with the majority of particles around 5 nm, only a few larger than 25 nm, and an average particle size of 12.4 nm. A larger particle size is beneficial for the perovskite material as smaller HOIP flakes tend to have a larger bandgap and increased charge recombination, which is in agreement with the ref [61], leading to decreased short-circuit current and device efficiency.

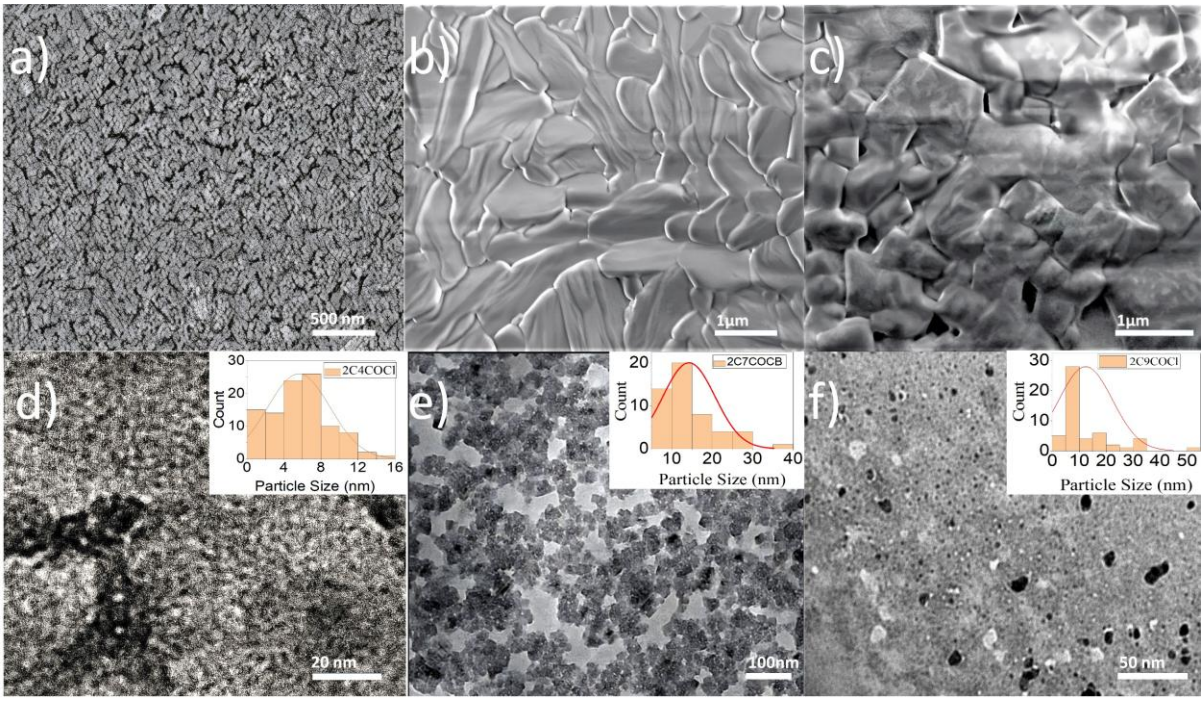

Figure 3: (a) SEM images depicting the morphology of Co-based perovskite films. short-chain 2C4CoC (b, c) The surface morphology of with medium and long organic chains (2C7CoCB, 2C9CoCl). The images illustrate the surface characteristics of spin-coated Co-based layers on glass substrates. (d) Transmission electron microscopy (TEM) images of short-chain perovskite with insets illustrating the particle size. (e, f) TEM images show crystals of Co-based perovskite (2C7CoCB, 2C9CoCl) with insets demonstrating the particle sizes.

3.3 Optical and electrical properties

3.3.1 Transmissions measurement & bandgap

Figure 4 (a) shows the transmission spectrum (280 to 1200 nm) of spin-coated Co-based perovskite thin films (measured at 420 nm thickness using SEM) on a glass substrate. The absorption peak observed at 682 nm can be attributed to the tetrahedral coordination of [CoCl4] [62], [63] Notably, the 2C9CoCl sample demonstrates higher light absorption compared to 2C4CoCl, aligning with previous findings that HOIPs with longer organic chains exhibit superior absorption capabilities [16], [64]. The absorption further increases when a combination of chloride and bromide anions is used, as seen in the case of 2C7CoCB. This observation supports the notion that introducing bromide leads to increased absorbance, a phenomenon observed in other perovskite materials [65], it suggests that the molar absorption coefficient rises as the Cl content decreases in the $A_2B(Cl_xBr_{1-x})$ structure.

In Figure 4 (b), present the bandgap calculation using the Kubelka-Munk equation. The extrapolation of the linear region and its intersection with the Y-axis provides the bandgap energy (Eg) for direct transitions. The Co-based perovskite hybrid materials exhibit bandgaps ranging from approximately 1.7 to 2.7 eV. A decrease in bandgap energy is observed with an increase in the length of the organic chain and the introduction of Br ions. This results in bandgap values of approximately 2.7 eV for 2C4CoCl, 2.2 eV for 2C9CoCl, and a promising value of 1.7 eV for 2C7CoCB. These findings indicate the possibility of achieving a more suitable bandgap for photovoltaic applications (theoretical optimum at 1.2 eV) by incorporating bromide and utilizing longer organic chains. Moreover, longer organic chains can enhance the transport properties as the hydrogen bonds between the organic and inorganic components contribute to charge transport within the molecules.

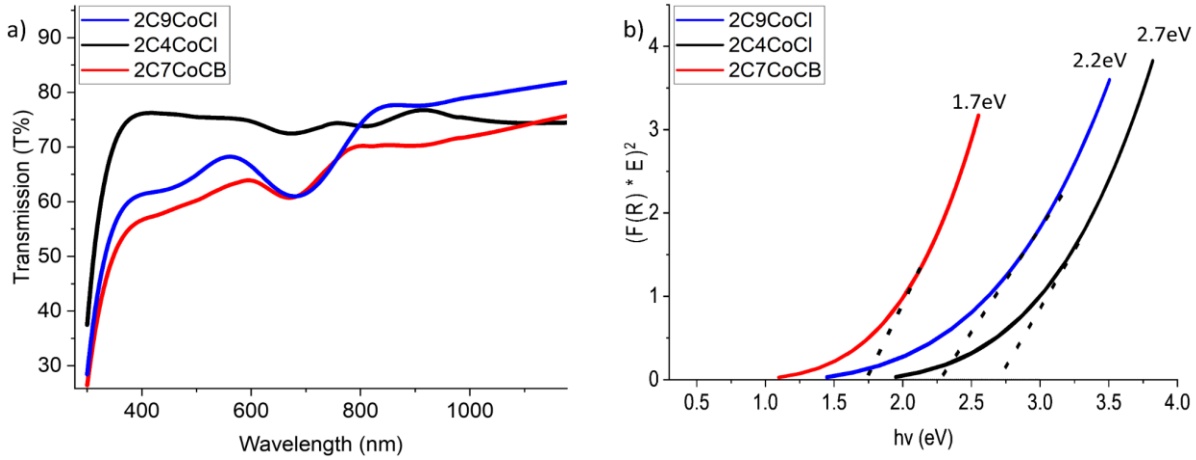

Figure 4: (a) UV-vis Transmission spectra for Co-based perovskite. (b) bandgap energy calculation.

3.3.2 Current- Voltage measurement (J-V) curve

Architecture 1

The performance of Co-based HOIP devices is significantly influenced by the deposition method employed during fabrication, as discussed earlier. Architecture 1 involves the deposition of the perovskite material within a mesoporous TiO_2 layer, situated between a carbon electrode and a ZrO_2 spacer. Figure (5) illustrates the current-voltage (I-V) characteristics of three compositions in solar cells measuring 11 x 9 mm (= 99 mm^2). In Figure 5 (a), the perovskite solar cell based on 2C4CoCl showed a Voc of 0.52 V and a Jsc of 0.52 mA/cm^2, yielding an efficiency of 0.151 % and a fill factor of 60 %. The solar cell utilizing the long-chain equivalent, 2C9CoCl HOIP, exhibited similar values with a slightly lower Voc of 0.49 V and a Jsc of 0.52 mA/cm^2. The efficiency remained consistent at 0.156 %, and the fill factor was 61 %. Additionally, the 2C7CoCB solar cell demonstrated a Voc of 0.44 V and

a Jsc of 0.54 mA/cm^2, leading to an efficiency of 0.16 % and a fill factor of 67 %. Figure 5 (b) presents the reverse characteristics, which showed an improvement in the aforementioned values, yielding an efficiency of 0.17 %. Table 3 provides a comprehensive overview of both the forward and reverse characteristics.

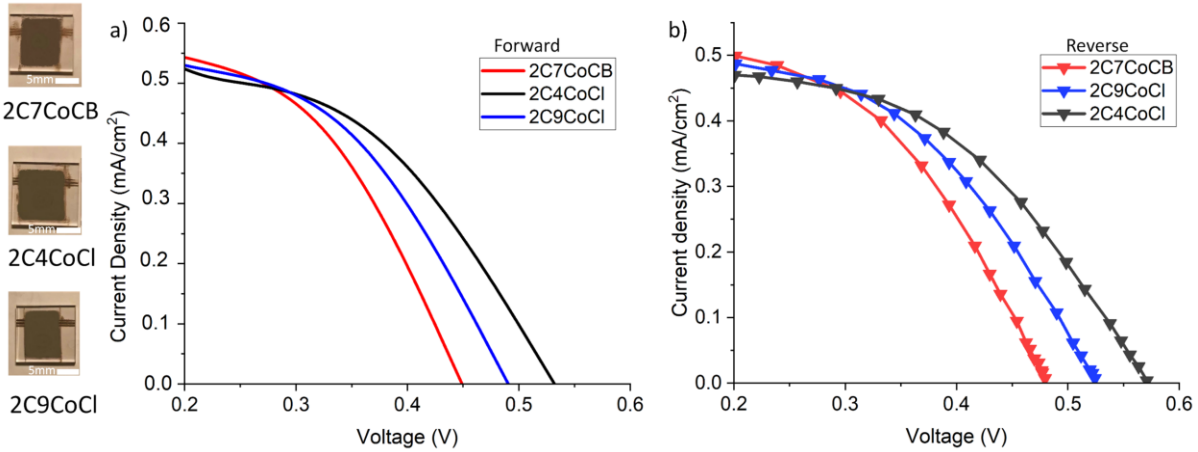

Figure 5: Current–Voltage [*J–V*] curves for three CO-based structures represent deposition Architecture1. (a) Forward scan. (b) Reverse.

Architecture 2

Figure 6 (a) illustrates the current-voltage (I-V) characteristics of solar cells fabricated using the three different cobalt-based materials with Architecture 2. The solar cells had dimensions of 4 x 4 mm (=16 mm^2). The 2C4CoCl device demonstrated a Voc of 0.96 V and a Jsc of 0.24 mA/cm^2, resulting in an efficiency of 0.43 % and a fill factor of 69 %. Upon increasing the length of the organic chain for the 2C9CoCl device, the Voc decreased to 0.95 V, while the Jsc remained at 0.24 mA/cm^2. However, an improvement in the fill factor (72 %) led to a slight enhancement in efficiency (0.44 %). Finally, the 2C7CoCB device achieved a Voc of 0.93 V and a Jsc of 0.24 mA/cm^2, resulting in an efficiency of 0.47 % and a fill factor of 78 % in the forward scan. The reverse scan in Figure 6(b) displayed a slight increase in efficiency values, reaching approximately 0.48 %.

A comparison of the I-V characteristics between the two deposition approaches revealed notable differences in performance. The conventional Architecture exhibited a lower Jsc, indicating a lower efficiency in converting photons to electrical energy. Additionally, an increase in Voc was observed, suggesting current loss due to transport and electron layer material hysteresis. Conversely, the first approach, deposition Architecture, yielded a higher Jsc and lower Voc, indicating a higher efficiency in converting photons to electrical energy. The reduction in Voc was attributed to the decrease in bandgap resulting from an increased halide composition, enabling the absorption of a greater number of photons by the material. Hole transporter-free configurations exhibited lower voltage and fill factor compared to other perovskite solar cell architectures due to the absence of a hole transport layer (HTL)

and the requirement for holes to travel longer distances through the ZrO_2 and carbon mesoporous layers. These results underscore the significance of selecting an appropriate deposition Architecture for the development of high-performance Co-based perovskite devices.

Hysteresis in the transport and electron layer material was observed in both configurations, albeit with varying effects on the results. The average hysteresis was calculated as 0.08 for Architecture 1 and 0.02 for Architecture 2. Hysteresis can arise from various factors, such as non-uniformity in material composition and film defects due to ion accumulation during the opposite polarization. [66], [67], or the presence of impurities [66]. These factors can introduce variations in the (Jsc, Voc) characteristics of the device under different operational conditions. By contrast, in architecture 2, the steady Jsc suggests that factors other than photon absorption, such as charge carrier transport through the material, limit the current output. Conversely, the increase in Voc indicates an accumulation of charge carriers at the interface between the perovskite and the transport layer. This accumulation leads to an augmented built-in potential and a subsequent decrease in current output. These findings align with previous studies that have reported a correlation between hysteresis and the accumulation of charge carriers at the interface [68].

The disparities observed in the I-V characteristics between the two deposition approaches can be attributed to variations in photon recombination. In Architecture 1, the inclusion of higher halide compositions results in a reduction of the bandgap, enabling increased photon absorption by the Co-perovskite material. This, in turn, leads to an elevation in Jsc and a decline in Voc, indicating that more electrons transition into the conductive band of the perovskite material prior to recombination. These outcomes are consistent with the findings reported in reference [69]. However, it is worth noting that the carbon electrode and ZrO_2 spacer are probable sites for charge carrier recombination, as the perovskite material is grown within the mesoporous TiO_2 layer. This may impose limitations on the device overall efficiency.

The choice of deposition architecture can significantly impact the performance of Co-based perovskite devices. By precisely controlling the deposition conditions and optimizing the material composition, it is possible to achieve higher-performance devices with improved efficiency and stability. Co-based perovskite solar cells may exhibit similar behaviours to other 2D-based perovskites, such as Bi-based perovskites, which have demonstrated enhanced efficiency [32], This suggests that similar characteristics and improvements can be anticipated in both types of perovskites. Table 3 provides summary of the I-V characteristics of the Co-based solar cell prepared by both deposition techniques employed in this study.

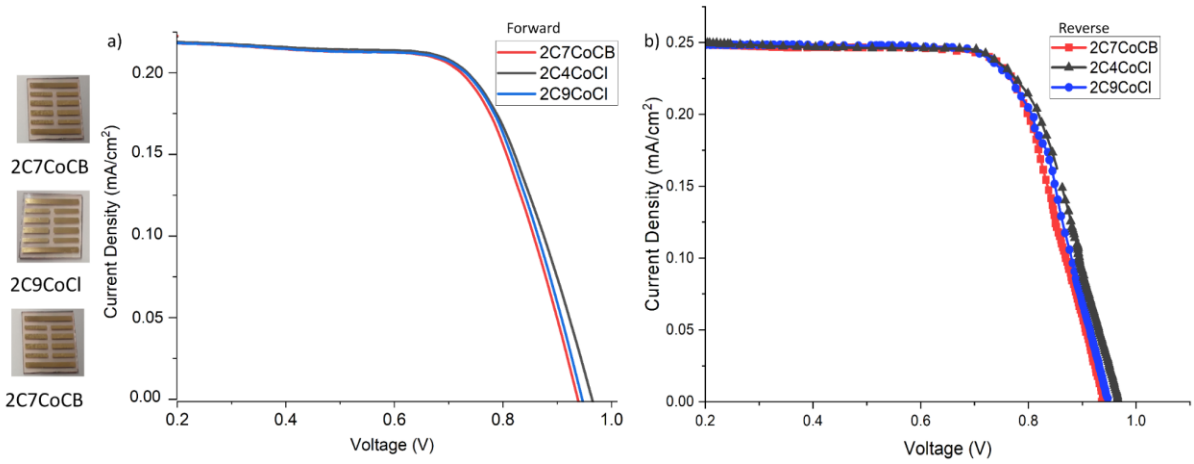

Figure 6: Current–Voltage [*J*–*V*] curves for three Co-based structures with deposition Architecture 2. (a) forward scan, and (b) reverse scan.

Table 3: Electrical characteristics of the solar cells.

Composition		Architecture 1				Architecture 2			
		V_{OC}	J_{SC} (mA/cm^2)	FF %	η%	V_{OC}	J_{SC} (mA/cm^2)	FF%	η%
2C4CoCl	Forward	0.52	0.52	60	0.151	0.96	0.24	69	0.43
	Reverse	0.56	0.47	63	0.165	0.96	025	70	0.44
2C9CoCl	Forward	0.49	0.53	61	0.156	0.95	0.24	72	0.44
	Reverse	0.52	0.48	65	0.162	0.95	0.25	73	0.45
2C7CoCB	Forward	0.44	0.54	67	0.160	0.93	0.24	78	0.47
	Reverse	0.48	0.50	71	0.171	0.94	0.25	79	0.48

According to the results presented in Table 3, Co-based perovskites have exhibited significant potential for efficiency improvement, making them a focus of ongoing investigation in the field of photovoltaics. Ongoing efforts to optimize their structure and properties may lead to Co-based perovskites becoming a competitive and viable alternative to Pb-based solar cells. Notably, research has been conducted on Sn-based mixed halide PSC $MASnI_{3-x}Br_x$, demonstrating that the inclusion of Br content led to an increase in the energy band gap from 1.30 to 2.15 eV. Additionally, the introduction of Br ions resulted in an enhanced fill factor (FF), with values increasing from 0.48 for $CH_3NH_3SnI_3$ to 0.59 for $CH_3NH_3SnIBr_2$, thereby achieving an improved PCE from 4.44 % to 5.73 % [70].

These findings highlight the influence of halide anion variation on the photovoltaic performance of perovskite solar cells, which is highly relevant for Co-based perovskites. The efficiency gains observed in Table 3 further support the impact of including Br content. Moreover, literature reports indicate that Cs, MA, and FA halide perovskite materials have been explored for tin-based perovskite, leading to efficiency enhancements from 3.13 % for $MASnI_3$ to 5.51 % for $FASnI_3$ [71], [72]. This suggests that the utilization of different cations can also affect the properties of Co-based perovskite solar cells.

Furthermore, it has been observed that altering the chain length of organic cations in perovskite solar cells can influence their optical properties. For instance, $MA_2CuClBr_3$ exhibited an efficiency of 0.017 % and a bandgap of 1.80 eV [65]. These findings suggest that optimizing the chain length of organic cations in Co-based perovskite solar cells has the potential to improve their efficiency. Therefore, modifying the halide anion, employing different cations, and optimizing the chain length of organic cations all hold promise for enhancing the efficiency of Co-based perovskite solar cells [18], [21], [24], [25].

Co-based perovskites show promising possibilities for photovoltaics [45], [23]–[25]. This study focused on optimizing their structure and properties for achieving competitive performance. The 2D cobalt-based perovskites here presented offer a pathway for efficiency improvement through materials nanoarchitectonics, organic chain length modification and mixed halide anion composition via chemical synthesis, resulting in an efficiency of 0.48 % [73], [25]. However, exploration in this field remains relatively new compared to other materials, and there is room for improvement, especially when there is not a clear substitute for lead-based perovskites. Tin-based perovskites $MASnI_3$ and $FASnI_3$ achieve efficiencies exceeding 5%, but phase segregation and trap states impede further progress, and Sn-based perovskites face challenges due to their high vulnerability to oxidation by water and oxygen when compared to other perovskite materials, which limits their long-term performance [71]. Germanium-based perovskites $MAGeI_3$ exhibit improved chemical stability compared to tin, however, Ge-based perovskites suffer from limitations in charge transport and bandgap optimization, hindering their efficiency improvement drawbacks in charge transport and suboptimal bandgaps hinder their efficiency to about 0.20 % [33]. Bismuth-based perovskites MA_3Bi2I_9 are attractive due to their favourable optical properties and as photovoltaic materials, but achieving high efficiencies and long-term stability remains a challenge as the material exhibits about 0.39% PCE. Bismuth-based perovskites are non-toxic and have favourable optical properties, but struggle achieving high efficiencies and long-term stability [43], [33]. Copper-based perovskites $(CH_3NH_3)_2CuCl_4$ offer a lower-toxicity alternative, but exhibit relatively low efficiencies and stability, necessitating structural modifications for improved performance, Cu-based perovskites, despite their low toxicity, require structural modifications to enhance stability and efficiency, presenting challenges in their application [65],[40].

Conclusion

In this study, an innovative fabrication of hybrid organic-inorganic perovskite solar cells utilizing cobalt-based compounds as an alternative to lead-based materials was investigated. Three variants of 2D-OIH Co-based perovskites, namely $[NH_3(CH_2)_nNH_3]CoCl_4$ (n = 4, 9) and $[NH_3(CH_2)_7NH3]CoBr_2Cl_2$, with varying organic chain lengths and halide compositions were examined. The research demonstrated that cobalt-based perovskites have the potential to mitigate environmental and human toxicity associated with conventional lead-based perovskites. To maximize efficiency, two different deposition architectures, employing chemical solutions and spin-coating techniques, were utilized for fabricating the device layers. The crystal structure was confirmed using single crystal XRD, whereas SEM provided insights into the morphology and TEM nanoparticle size. The optical properties were analysed, revealing that the length of organic cations could modulate the optical bandgap. Specifically, $[NH_3(CH_2)_9NH_3]CoCl_4$ exhibited an optical bandgap of approximately 2.2 eV, while $[NH_3(CH_2)_7NH_3]CoBr_2Cl_2$ displayed an optical bandgap of around 1.7 eV. J-V measurements were conducted for the three different perovskite materials. Architecture 2 deposition for $[NH3(CH_2)_7NH_3]CoBr_2Cl_2$ demonstrated the highest efficiency, reaching approximately 0.47 %. The solar cell exhibited an open circuit voltage of 0.93 V, a current density J_{SC} of 0.24 mA/cm^2, and a fill factor of 78 % during the forward scan. In contrast, Architecture 1 deposition for $[NH_3(CH_2)_7NH_3]CoBr_2Cl_2$ yielded an efficiency of 0.16 %. The solar cell achieved an open circuit voltage of 0.44 V, a current density J_{SC} of 0.54 mA/cm^2, and fill factor of 67 % during the forward scan. The utilization of different deposition architectures, along with the optimization of organic cation chain length, enables the fine-tuning of optical properties and enhances the overall device performance. This study presents cobalt-based hybrid perovskite solar cells could be transformative, environmentally friendly alternative to lead-based materials. The optimized deposition architectures and fine-tuned organic cation chain lengths showcased in this research hold practical promise, offering sustainable advancements in solar cell technology with broader implications for energy solutions.

Acknowledgement

Seham K. Abdel-Aal acknowledges Mujeres Por Africa Organization 6th edition for the fund and facilities provided by ICFO. MA and JMH acknowledge the funding of the Libyan Embassy in the UK (ref. 13691). J.M.H. thanks the Spanish Ministerio de Universidades for support through the program Beatriz Galindo (Award BG22/00128).

Author contribution

MA: Experimental, Architecture1 and manuscript writing; SA: HOIP synthesis, material characterization and Architecture 2; CAB.: experimental and editing; DR: review and supervision (Architecture 2); FBT: experimental (Architecture 2); KLW: experimental (Architecture 1); DPH:

resources; JM: resources, supervision; JMH: Project administration, supervision and writing. All the authors reviewed and edited the final draft.

Conflict of interest

The authors declare that they have no conflict of interest.

Data availability

Data will be made available at reasonable request.

References

[1] "National Renewable Energy Laboratory, https://www.nrel.gov/pv/assets/pdfs/best-research-cell-efficiencies-rev220630.," 2022. .

[2] Z. Song, S. C. Watthage, A. B. Phillips, and M. J. Heben, "Pathways toward high-performance perovskite solar cells: review of recent advances in organo-metal halide perovskites for photovoltaic applications," *J Photonics Energy*, vol. 6, no. 2, p. 022001, 2016, doi: 10.1117/1.jpe.6.022001.

[3] K. P. Bhandari and R. J. Ellingson, *An Overview of Hybrid Organic–Inorganic Metal Halide Perovskite Solar Cells*. Cambridge, Massachusetts : Elsevier, 2018.

[4] S. Kundu and T. L. Kelly, "In situ studies of the degradation mechanisms of perovskite solar cells," *EcoMat*, vol. 2, no. 2, pp. 1–22, 2020, doi: 10.1002/eom2.12025.

[5] M. Ikram *et al.*, "Recent advancements and future insight of lead-free non-toxic perovskite solar cells for sustainable and clean energy production: A review," *Sustain Energy Technol Assessments*, vol. 53, no. PA, p. 102433, 2022, doi: 10.1016/j.seta.2022.102433.

[6] C. Zhang *et al.*, "Development of a mixed halide-chalcogenide bismuth-based perovskite MABiI 2 S with small bandgap and wide absorption range," *Chem Lett*, vol. 48, no. 3, pp. 249–252, 2019, doi: 10.1246/cl.180919.

[7] P. V. Kamat, J. Bisquert, and J. Buriak, "Lead-free perovskite solar cells," *ACS Energy Lett*, vol. 2, no. 4, pp. 904–905, 2017, doi: 10.1021/acsenergylett.7b00246.

[8] H. Li *et al.*, "Perovskite catalysts with different dimensionalities for environmental and energy applications: A review," *Sep Purif Technol*, vol. 307, no. November 2022, p. 122716, 2023, doi: 10.1016/j.seppur.2022.122716.

[9] Y. Jiang *et al.*, "Reduced-Dimensional α-CsPbX3 Perovskites for Efficient and Stable Photovoltaics," *Joule*, vol. 2, no. 7, pp. 1356–1368, 2018, doi: 10.1016/j.joule.2018.05.004.

[10] B. Do Lee, J. W. Lee, M. Kim, W. B. Park, and K. S. Sohn, “Discovery of Pb-free hybrid organic–inorganic 2D perovskites using a stepwise optimization strategy,” *npj Comput Mater*, vol. 8, no. 1, pp. 1–12, 2022, doi: 10.1038/s41524-022-00781-z.

[11] X. Zhang *et al.*, “Stable high efficiency two-dimensional perovskite solar cells via cesium doping,” *Energy Environ Sci*, vol. 10, no. 10, pp. 2095–2102, 2017, doi: 10.1039/c7ee01145h.

[12] H. Li *et al.*, “Two-Dimensional Metal-Halide Perovskite-based Optoelectronics: Synthesis, Structure, Properties and Applications,” *Energy Environ Mater*, vol. 4, no. 1, pp. 46–64, 2021, doi: 10.1002/eem2.12087.

[13] T. Zhu and X. Gong, “Low-dimensional perovskite materials and their optoelectronics,” *InfoMat*, vol. 3, no. 10, pp. 1039–1069, 2021, doi: 10.1002/inf2.12211.

[14] X. Gao *et al.*, “Ruddlesden–Popper Perovskites: Synthesis and Optical Properties for Optoelectronic Applications,” *Advanced Science*, vol. 6, no. 22. 2019, doi: 10.1002/advs.201900941.

[15] K. Wang, J. Y. Park, Akriti, and L. Dou, “ Two-dimensional halide perovskite quantum-well emitters: A critical review ,” *EcoMat*, vol. 3, no. 3, pp. 1–13, 2021, doi: 10.1002/eom2.12104.

[16] S. K. Abdel-Aal, G. Kocher-Oberlehner, A. Ionov, and R. N. Mozhchil, “Effect of organic chain length on structure, electronic composition, lattice potential energy, and optical properties of 2D hybrid perovskites [(NH3)(CH2)n(NH3)]CuCl4, n = 2–9,” *Appl Phys A Mater Sci Process*, vol. 123, no. 8, pp. 1–10, 2017, doi: 10.1007/s00339-017-1150-8.

[17] M. F. Mostafa, S. S. El-khiyami, and S. K. Abd-elal, “Crystal structure , phase transition and conductivity study of two new organic e inorganic hybrids : [(CH 2) 7 (NH 3) 2] X 2 , X ¼ Cl / Br,” *J Mol Struct*, vol. 1127, pp. 59–73, 2017, doi: 10.1016/j.molstruc.2016.07.025.

[18] S. K. Abdel-aal and A. S. Abdel-rahman, “Synthesis , structure , lattice energy and enthalpy of 2D hybrid,” vol. 457, pp. 282–288, 2017, doi: 10.1016/j.jcrysgro.2016.08.006.

[19] Y. Chen, Y. Sun, J. Peng, J. Tang, K. Zheng, and Z. Liang, “2D Ruddlesden–Popper Perovskites for Optoelectronics,” *Adv Mater*, vol. 30, no. 2, 2018, doi: 10.1002/adma.201703487.

[20] S. K. Abdel-Aal, M. Harfouche, A. Ouasri, and A. S. Abdel-Rahman, “Crystal structures, Hirshfeld surfaces, Infrared, and XRF/XAFS studies of Long-chain 2D Lead-free Hybrid Perovskite NH3(CH2)9NH3MCl4 (M = Mn, Co, Cu),” *J Mol Struct*, vol. 1276, p. 134757, 2023, doi: 10.1016/j.molstruc.2022.134757.

[21] S. K. Abdel-Aal and A. S. Abdel-Rahman, “Synthesis, structure, lattice energy and enthalpy of

2D hybrid perovskite [NH3(CH2)4NH3]CoCl4, compared to [NH3(CH2)nNH3]CoCl4, n=3–9," *J Cryst Growth*, vol. 457, pp. 282–288, 2017, doi: 10.1016/j.jcrysgro.2016.08.006.

[22] S. K. Abdel-Aal, G. Bortel, Pekker, K. Kamarás, G. Faigel, and A. S. Abdel-Rahman, "Structure investigation and vibrational spectroscopy of two prospective hybrid perovskites based on Mn and Co," *J Phys Chem Solids*, vol. 161, no. October 2021, 2022, doi: 10.1016/j.jpcs.2021.110400.

[23] M. F. Mostafa, S. S. El-khiyami, and S. K. Alal, "Structure, thermal, and impedance study of a new organic–inorganic hybrid [(CH2)7(NH3)2]CoCl4," *J Phys Chem Solids*, vol. 118, no. February, pp. 6–13, 2018, doi: 10.1016/j.jpcs.2018.02.048.

[24] M. F. Mostafa, S. Abd-Elal, and A. K. Tammam, "Crystal structure, thermal, electric and magnetic study of [(CH 2)7(NH3)2]CoCl2Br 2," *Indian J Phys*, vol. 88, no. 1, pp. 49–57, 2014, doi: 10.1007/s12648-013-0371-8.

[25] S. K. Abdel-Aal and A. Ouasri, "Crystal structure, Hirshfeld surfaces and vibrational studies of tetrachlorocobaltate hybrid perovskite salts NH3(CH2)nNH3CoCl4 (n = 4, 9)," *J Mol Struct*, vol. 1251, p. 131997, 2022, doi: 10.1016/j.molstruc.2021.131997.

[26] M. F. Mostafa, S. S. Elkhiyami, and S. A. Alal, "Discontinuous transition from insulator to semiconductor induced by phase change of the new organic- inorganic hybrid [(CH2)7(NH3)2]CoBr4," *Mater Chem Phys*, vol. 199, pp. 454–463, 2017, doi: 10.1016/j.matchemphys.2017.07.041.

[27] T. Zhu, Y. Yang, and X. Gong, "Recent Advancements and Challenges for Low-Toxicity Perovskite Materials," 2020, doi: 10.1021/acsami.0c02575.

[28] M. Kar, R. Sarkar, S. Pal, and P. Sarkar, "Lead Free Two-Dimensional Mixed Tin and Germanium Halide Perovskites for Photovoltaic Applications," 2021, doi: 10.1021/acs.jpcc.0c08164.

[29] L. F. Photovoltaic, P. Applications, L. Ma, M. Ju, and X. Cheng, "Tin and Germanium Based Two-dimensional Tin and Germanium Based Two-dimensional Ruddlesden − Popper Hybrid Perovskites for Potential Lead − Free Photovoltaic and Photoelectronic Applications †," 2018, doi: 10.1039/x0xx00000x.

[30] W. Ke, C. C. Stoumpos, and M. G. Kanatzidis, "' Unleaded ' Perovskites : Status Quo and Future Prospects of Tin-Based Perovskite Solar Cells," vol. 1803230, 2019, doi: 10.1002/adma.201803230.

[31] M. Leng *et al.*, "Surface Passivation of Bismuth-Based Perovskite Variant Quantum Dots To

Achieve E ffi cient Blue Emission," 2018, doi: 10.1021/acs.nanolett.8b03090.

[32] Y. Cui, L. Yang, X. Wu, J. Deng, X. Zhang, and J. Zhang, "Recent progress of lead-free bismuth-based perovskite materials for solar cell applications," *J Mater Chem C*, vol. 13, no. 9, pp. 16629–16656, 2022, doi: 10.1039/d2tc02643k.

[33] R. Ali, G. J. Hou, Z. G. Zhu, Q. B. Yan, Q. R. Zheng, and G. Su, "Predicted Lead-Free Perovskites for Solar Cells," *Chem Mater*, vol. 30, no. 3, pp. 718–728, 2018, doi: 10.1021/acs.chemmater.7b04036.

[34] G. E. Eperon, S. D. Stranks, C. Menelaou, M. B. Johnston, L. M. Herz, and H. J. Snaith, "Formamidinium lead trihalide: A broadly tunable perovskite for efficient planar heterojunction solar cells," *Energy Environ Sci*, vol. 7, no. 3, pp. 982–988, 2014, doi: 10.1039/c3ee43822h.

[35] L. Liang and P. Gao, "Lead-Free Hybrid Perovskite Absorbers for Viable Application: Can We Eat the Cake and Have It too?," *Adv Sci*, vol. 5, no. 2, 2018, doi: 10.1002/advs.201700331.

[36] I. Kopacic *et al.*, "Enhanced Performance of Germanium Halide Perovskite Solar Cells through Compositional Engineering," *ACS Appl Energy Mater*, vol. 1, no. 2, pp. 343–347, 2018, doi: 10.1021/acsaem.8b00007.

[37] P. Cheng, T. Wu, J. Liu, W. Q. Deng, and K. Han, "Lead-Free, Two-Dimensional Mixed Germanium and Tin Perovskites," *J Phys Chem Lett*, vol. 9, no. 10, pp. 2518–2522, 2018, doi: 10.1021/acs.jpclett.8b00871.

[38] A. Leo *et al.*, "Copper oxide - perovskite mixed matrix membranes delivering very high oxygen fl uxes," *J Memb Sci*, vol. 526, no. August 2016, pp. 323–333, 2017, doi: 10.1016/j.memsci.2016.12.035.

[39] A. Abate, "Perovskite Solar Cells Go Lead Free," *Joule*, vol. 1, no. 4, pp. 659–664, 2017, doi: 10.1016/j.joule.2017.09.007.

[40] S. F. Hoefler, G. Trimmel, and T. Rath, "Progress on lead-free metal halide perovskites for photovoltaic applications: a review," *Monatshefte fur Chemie*, vol. 148, no. 5, pp. 795–826, 2017, doi: 10.1007/s00706-017-1933-9.

[41] A. M. Elseman, A. E. Shalan, S. Sajid, M. M. Rashad, A. M. Hassan, and M. Li, "Copper-Substituted Lead Perovskite Materials Constructed with Different Halides for Working (CH3NH3)2CuX4-Based Perovskite Solar Cells from Experimental and Theoretical View," *ACS Appl Mater Interfaces*, vol. 10, no. 14, pp. 11699–11707, 2018, doi: 10.1021/acsami.8b00495.

[42] R. Kour *et al.*, “Potential Substitutes for Replacement of Lead in Perovskite Solar Cells: A Review,” *Glob Challenges*, vol. 3, no. 11, p. 1900050, 2019, doi: 10.1002/gch2.201900050.

[43] F. Li, H. Fan, P. Wang, X. Li, Y. Song, and K. J. Jiang, “Improved film morphology of (CH 3 NH 3) 3 Bi 2 I 9 via cation displacement approach for lead-free perovskite solar cells,” *J Mater Sci*, vol. 54, no. 14, pp. 10371–10378, 2019, doi: 10.1007/s10853-019-03582-w.

[44] M. Adnan and J. K. Lee, “All Sequential Dip-Coating Processed Perovskite Layers from an Aqueous Lead Precursor for High Efficiency Perovskite Solar Cells,” *Sci Rep*, vol. 8, no. 1, pp. 1–10, 2018, doi: 10.1038/s41598-018-20296-2.

[45] M. T. Klug *et al.*, “Tailoring metal halide perovskites through metal substitution: Influence on photovoltaic and material properties,” *Energy Environ Sci*, vol. 10, no. 1, pp. 236–246, 2017, doi: 10.1039/c6ee03201j.

[46] Y. Chen, M. He, J. Peng, Y. Sun, and Z. Liang, “Structure and growth control of organic–inorganic halide perovskites for optoelectronics: From polycrystalline films to single crystals,” *Adv Sci*, vol. 3, no. 4, 2016, doi: 10.1002/advs.201500392.

[47] R. Swartwout, M. T. Hoerantner, and V. Bulovi, “Scalable Deposition Methods for Large-Area Production of Perovskite Thin Films,” pp. 119–145, 2019, doi: 10.1002/eem2.12043.

[48] Y. Chen, M. Zhang, F. Li, and Z. Yang, “Recent Progress in Perovskite Solar Cells : Status and Future layer,” 2023.

[49] J. Im, J. Chun, S. Kim, and N. Park, “of a nanocrystalline 2H perovskite-type novel Synthesis , structure , and photovoltaic property of a nanocrystalline 2H perovskite-type novel,” *Nanoscale Res Lett*, vol. 7, no. 1, p. 353, 2012, [Online]. Available: Nanoscale Research Letters.

[50] C. Zhang *et al.*, “Influence of different TiO 2 blocking films on the photovoltaic performance of perovskite solar cells,” *Appl Surf Sci*, vol. 388, pp. 82–88, 2016, doi: 10.1016/j.apsusc.2016.03.093.

[51] Z. Ku, Y. Rong, M. Xu, T. Liu, and H. Han, “Full printable processed mesoscopic CH3 NH3 PbI 3 /TiO2 heterojunction solar cells with carbon counter electrode,” *Sci Rep*, vol. 3, 2013, doi: 10.1038/srep03132.

[52] N. F. Ramli *et al.*, “Compatibility between compact and mesoporous TiO2 layers on the optimization of photocurrent density in photoelectrochemical cells,” *Surfaces and Interfaces*, vol. 17, no. May, p. 100341, 2019, doi: 10.1016/j.surfin.2019.100341.

[53] M. S. Prasad, B. Mallikarjun, M. Ramakrishna, J. Joarder, B. Sobha, and S. Sakthivel,

"Zirconia nanoparticles embedded spinel selective absorber coating for high performance in open atmospheric condition," *Sol Energy Mater Sol Cells*, vol. 174, no. September 2017, pp. 423–432, 2018, doi: 10.1016/j.solmat.2017.09.032.

[54] Y. Li *et al.*, "Effect of ZrO 2 film thickness on the photoelectric properties of mixed-cation perovskite solar cells," *Appl Surf Sci*, vol. 439, pp. 506–515, 2018, doi: 10.1016/j.apsusc.2018.01.005.

[55] R. Dileep *et al.*, "Room-temperature curable carbon cathode for hole-conductor free perovskite solar cells," *Sol Energy*, vol. 187, no. May, pp. 261–268, 2019, doi: 10.1016/j.solener.2019.05.045.

[56] R. Dileep *et al.*, "Room-temperature curable carbon cathode for hole-conductor free perovskite solar cells," *Sol Energy*, vol. 187, no. March, pp. 261–268, 2019, doi: 10.1016/j.solener.2019.05.045.

[57] X. Y. b and S. Y. Meidan Que, Boyue Zhang, Jin Chen, "Carbon-based electrodes for perovskite solar cells," *Mater Adv*, pp. 5560–5579, 2021, doi: 10.1039/d1ma00352f.

[58] L. Zhou, Y. Zuo, T. K. Mallick, and S. Sundaram, "Enhanced Efficiency of Carbon-Based Mesoscopic Perovskite Solar Cells through a Tungsten Oxide Nanoparticle Additive in the Carbon Electrode," *Sci Rep*, vol. 9, no. 1, pp. 1–8, 2019, doi: 10.1038/s41598-019-45374-x.

[59] L. Cheng *et al.*, "Multiple-Quantum-Well Perovskites for High-Performance Light-Emitting Diodes," *Adv Mater*, vol. 32, no. 15, pp. 1–9, 2020, doi: 10.1002/adma.201904163.

[60] J. Li *et al.*, "Sodium bromide additive improved film morphology and performance in perovskite light-emitting diodes," *Appl Phys Lett*, vol. 111, no. 5, 2017, doi: 10.1063/1.4997325.

[61] Y. H. Kim *et al.*, "Highly Efficient Light-Emitting Diodes of Colloidal Metal-Halide Perovskite Nanocrystals beyond Quantum Size," *ACS Nano*, vol. 11, no. 7, pp. 6586–6593, 2017, doi: 10.1021/acsnano.6b07617.

[62] J. C. and S. G. Nemanja Banić, Milan Vraneš, Biljana Abramović, "Thermochromism, stability and thermodynamics of cobalt(II) complexes in newly synthesized nitrate based ionic liquid and its photostability," vol. 43, pp. 15515–15525, 2014, doi: 10.1039/c4dt01836b.

[63] J. C. and S. G. Nemanja Banić, Milan Vraneš, Biljana Abramović, "based ionic liquid and its photostability," pp. 15515–15525, 2014, doi: 10.1039/c4dt01836b.

[64] M. A. Green, Y. Jiang, A. Mahboubi, and A. Ho-baillie, "Optical Properties of Photovoltaic Organic − Inorganic Lead Halide Perovskites," 2015, doi: 10.1021/acs.jpclett.5b01865.

[65] D. Cortecchia *et al.*, “Lead-Free MA2CuClxBr4-x Hybrid Perovskites,” *Inorg Chem*, vol. 55, no. 3, pp. 1044–1052, 2016, doi: 10.1021/acs.inorgchem.5b01896.

[66] Q. Wali *et al.*, “Fundamentals of Hysteresis in Perovskite Solar Cells: From Structure-Property Relationship to Neoteric Breakthroughs,” *Chem Rec*, vol. 22, no. 1, 2022, doi: 10.1002/tcr.202100150.

[67] S. N. Habisreutinger, N. K. Noel, and H. J. Snaith, “Hysteresis Index: A Figure without Merit for Quantifying Hysteresis in Perovskite Solar Cells,” *ACS Energy Lett*, vol. 3, no. 10, pp. 2472–2476, 2018, doi: 10.1021/acsenergylett.8b01627.

[68] D. H. Kang and N. G. Park, “On the Current–Voltage Hysteresis in Perovskite Solar Cells: Dependence on Perovskite Composition and Methods to Remove Hysteresis,” *Adv Mater*, vol. 31, no. 34, pp. 1–23, 2019, doi: 10.1002/adma.201805214.

[69] N. K. Elumalai and A. Uddin, “Open circuit voltage of organic solar cells: An in-depth review,” *Energy Environ Sci*, vol. 9, no. 2, pp. 391–410, 2016, doi: 10.1039/c5ee02871j.

[70] F. Hao, C. C. Stoumpos, D. H. Cao, R. P. H. Chang, and M. G. Kanatzidis, “Lead-free solid-state organic-inorganic halide perovskite solar cells,” *Nat Photonics*, vol. 8, no. 6, pp. 489–494, 2014, doi: 10.1038/nphoton.2014.82.

[71] L. Peng and W. Xie, “Theoretical and experimental investigations on the bulk photovoltaic effect in lead-free perovskites MASnI3 and FASnI3,” *RSC Adv*, vol. 10, no. 25, pp. 14679–14688, 2020, doi: 10.1039/d0ra02584d.

[72] C. Gai, J. Wang, Y. Wang, and J. Li, “The Low-Dimensional Three-Dimensional Tin Halide Perovskite: Film Characterization and Device Performance,” *Energies*, vol. 13, no. 1, p. 2, 2019, doi: 10.3390/en13010002.

[73] K. Ariga and R. Fakhrullin, “Materials Nanoarchitectonics from Atom to Living Cell: A Method for Everything,” *Bull Chem Soc Jpn*, vol. 95, no. 5, pp. 774–795, 2022, doi: 10.1246/bcsj.20220071.